

Multi-Carrier Agile Phased Array Radar

Tianyao Huang, Nir Shlezinger, Xingyu Xu, Dingyou Ma, Yimin Liu, and Yonina C. Eldar

Abstract—Modern radar systems are expected to operate reliably in congested environments under cost and power constraints. A recent technology for realizing such systems is frequency agile radar (FAR), which transmits narrowband pulses in a frequency hopping manner. To enhance the target recovery performance of FAR in complex electromagnetic environments, we propose two radar schemes extending FAR to multi-carrier waveforms. The first is Wideband Multi-carrier Agile Radar (WMAR), which transmits/receives wideband waveforms simultaneously with every antenna. To avoid the increased cost associated with wideband waveforms used by WMAR, we next propose multi-Carrier Agile phaSed Array Radar (CAESAR). CAESAR uses narrowband monotone waveforms, thus reducing system complexity significantly, while introducing *spatial agility*. We characterize the transmitted and received signals of the proposed schemes, and develop an algorithm for recovering the targets, which combines concepts from compressed sensing to estimate the range-Doppler parameters of the targets. We derive conditions which guarantee their accurate reconstruction. Our numerical study demonstrates that both multi-carrier schemes improve performance compared to conventional FAR while maintaining its practical benefits. We also demonstrate that the performance of CAESAR, which uses monotone waveforms, is within a small gap from the more costly wideband radar.

I. INTRODUCTION

Emerging technologies, such as autonomous vehicles, introduce new challenges for radar systems. Modern radars must be reliable, but at the same time compact, flexible, robust, and efficient in terms of cost and power usage [1]–[5]. A possible approach to meet these requirements is by exploiting *frequency agility* [1], namely, to utilize narrowband waveforms, while allowing the carrier frequencies to vary between different radar pulses. Frequency agile radar (FAR) was shown to achieve excellent electronic counter-countermeasures (ECCM) and electromagnetic compatibility (EMC) performance [1], and has the flexibility of supporting spectrum sharing [5]. Furthermore, FAR is compatible with conventional widespread phased array antennas. Finally, by utilizing narrowband signals with varying frequencies, FAR systems can synthesize a large bandwidth with narrowband waveforms [2], [6], which reduces the hardware cost significantly, allowing the use of non-linear amplifiers without limiting their power efficiency.

A major drawback of FAR compared to wideband radar is its reduced range-Doppler reconstruction performance of targets. This reduced performance is a byproduct of the relatively small number of radar measurements processed by FAR,

Parts of this work were presented in the 2018 IEEE International Workshop on Compressed Sensing applied to Radar, Multimodal Sensing, and Imaging (CoSeRa). This work received funding from the National Natural Science Foundation of China under Grants 61571260 and 61801258, from the European Unions Horizon 2020 research and innovation program under grant No. 646804-ERC-COG-BNYQ, and from the Air Force Office of Scientific Research under grant No. FA9550-18-1-0208.

T. Huang, Y. Liu, X. Xu, and D. Ma are with the EE Department, Tsinghua University, Beijing, China (e-mail: {huangtianyao, yiminliu}@tsinghua.edu.cn; {xy-xu15, mdy16}@mails.tsinghua.edu.cn).

N. Shlezinger and Y. C. Eldar are with the Faculty of Math and CS, Weizmann Institute of Science, Rehovot, Israel (e-mail: nirshlezinger1@gmail.com; yonina.eldar@weizmann.ac.il).

which stems from its usage of a single narrowband waveform for each pulse. The performance reduction can be relieved by using compressed sensing (CS) algorithms that exploit sparsity of the target scheme [7]. However, the degradation becomes notable in extremely congested or contested electromagnetic environments [8], where there may be no vacant bands in some pulses or some radar returns of the transmitted pulses may be discarded due to strong interference [9], [10].

The performance degradation of FAR can be mitigated by using multi-carrier transmissions. When multiple carriers are transmitted simultaneously in a single pulse, the number of radar measurements is increased, and the target reconstruction performance is improved. Various multi-carrier radar schemes have been studied in the literature, including frequency division multiple access multiple-input multiple-output (FDMA-MIMO) [11], sub-Nyquist MIMO radar (SUMMeR) [12], and frequency diversity array (FDA) radar [13], [14]. In the aforementioned schemes, different array elements transmit waveforms at different frequencies, usually forming an omnidirectional beam and illuminating a large field-of-view [15]. This degrades radar performance, especially in track mode, where a highly directional beam focusing on the target is preferred [15]. In addition, frequency agility is not exploited in FDMA-MIMO and FDA. The derivation of frequency agile multi-carrier schemes for phased array radar, which leads to a focused beam with high gain, is the focus of this work.

Here, we propose two multi-carrier agile phased array radar schemes. The first uses all the antenna elements to transmit a single waveform consisting of multiple carriers simultaneously in each pulse. Frequency agility is induced by randomly selecting the carriers utilized, resulting in a wideband multi-carrier agile radar (WMAR) scheme. While the increased number of carriers is shown to achieve improved reconstruction performance compared to conventional FAR [8], WMAR utilizes multiband signals, thus its implementation is more costly than that uses conventional narrowband monotones, and may suffer from envelope fluctuation [16].

To overcome the increased hardware complexity of using wideband waveforms, we next develop multi-Carrier Agile phaSed Array Radar (CAESAR), which combines frequency agility and *spatial agility*. Specifically, CAESAR selects a small number of carrier frequencies on each pulse and randomly allocates different carrier frequencies among its antenna elements, such that each array element transmits a narrowband constant modulus waveform. This approach facilitates the usage of low complexity hardware and avoids envelope fluctuation and power efficiency degradation when using non-linear power amplifiers. An illustration of this transmission scheme is depicted in Fig. 1. For each carrier frequency, delicate phase shifts on the corresponding sub-array elements are used to yield a directional transmit beam, allowing to illuminate the tracked target in a similar manner as conventional phased array radar. Despite the fact that only a sub-array antenna

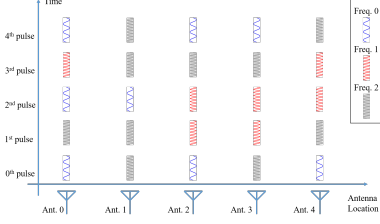


Fig. 1. Transmission example of CAESAR. In every pulse of this example, two out of three carrier frequencies are emitted by different sub-arrays. For example, frequency 0 and 2 are selected in the 0-th pulse and are sent by antenna 0, 2, 4 and antenna 1, 3, respectively. Traditional FAR or FDMA-MIMO/FDA can be regarded as a special case of CAESAR, with only one out of three frequencies or all available frequencies sent in each pulse.

is utilized for each frequency, the antenna-frequency hopping strategy of CAESAR results in array antenna gain loss and a relatively small performance gap compared to wideband radar equipped with the same antenna array. Furthermore, the combined randomization of frequency and antenna allocation can be exploited to realize a dual-function radar communication (DFRC) system [17]–[19] by embedding digital information into the selection of these parameters. We study the application of CAESAR as a DFRC system in a companion paper [20], and focus here on the radar and its performance.

To present WMAR and CAESAR, we characterize the signal model for each approach, based on which we develop a recovery algorithm for high-resolution range (HRR), Doppler, and angle estimation of radar targets. Our proposed algorithm utilizes CS methods for range-Doppler reconstruction, exploiting its underlying sparsity, and applies matched filtering to detect the angles of the targets. We provide a detailed theoretical analysis of the range-Doppler recovery performance of our proposed algorithm under complex electromagnetic environments. In particular, it is proved that CAESAR and WMAR are guaranteed to recover with high probability a number of scattering points which grows proportionally to the square root of the number of different narrowband signals used, i.e., the number of carrier frequencies that are simultaneously transmitted in each pulse. This theoretical result verifies that increasing the number of carriers improves target recovery, and reduces performance degradation due to intense interference in complex electromagnetic environments. WMAR and CAESAR are evaluated in a numerical study, where it is shown that their range-Doppler reconstruction performance as well as robustness to interference are substantially improved compared to conventional FAR. Additionally, it is demonstrated that the performance of CAESAR is only within a small gap from that achievable using costly wideband WMAR.

The remainder of the paper is structured as follows: Sections II and III present WMAR and CAESAR, respectively. Section IV introduces the recovery algorithm to estimate the range, Doppler, and angle of the targets. In Section V we discuss the pros and cons of each scheme compared to related radar methods. Section VI derives theoretical performance measures of the recovery method. Simulation results are presented in Section VII, and Section VIII concludes the paper.

Throughout the paper, we use \mathbb{C} , \mathbb{R} to denote the sets of complex, real numbers, respectively, and use $|\cdot|$ for the magnitude or cardinality of a scalar number, or a set,

respectively. Given $x \in \mathbb{R}$, $\lfloor x \rfloor$ denotes the largest integer less than or equal to x , and $\binom{n}{k} = \frac{n!}{k!(n-k)!}$ represents the binomial coefficient. Uppercase boldface letters denote matrices (e.g., \mathbf{A}), and boldface lowercase letters denote vectors (e.g., \mathbf{a}). The (n, m) -th element of matrix \mathbf{A} is denoted as $[\mathbf{A}]_{m,n}$, and similarly $[\mathbf{a}]_n$ is the n -th entry of the vector \mathbf{a} . Given a matrix $\mathbf{A} \in \mathbb{C}^{M \times N}$, and a number n (or a set of integers, Λ), $[\mathbf{A}]_n$ ($[\mathbf{A}]_\Lambda \in \mathbb{C}^{M \times |\Lambda|}$) is the n -th column of \mathbf{A} (the sub-matrix consisting of the columns of \mathbf{A} indexed by Λ). Similarly, $[\mathbf{a}]_\Lambda \in \mathbb{C}^{|\Lambda|}$ is the sub-vector consisting of the elements of $\mathbf{a} \in \mathbb{C}^N$ indexed by Λ . The complex conjugate, transpose, and the complex conjugate-transpose are denoted $(\cdot)^*$, $(\cdot)^T$, $(\cdot)^H$, respectively. Define $\|\cdot\|_p$ as the ℓ_p norm, $\|\cdot\|_0$ is the number of non-zero entries, and $\|\cdot\|_F$ is the Frobenius norm. The probability measure is $\mathbb{P}(\cdot)$, while $E[\cdot]$ and $D[\cdot]$ are the expectation and variance of a random argument, respectively.

II. WMAR

In this section we present the proposed WMAR scheme, which originates from FAR [1], aiming to increase the number of radar measurements and improve the range-Doppler recovery performance. We first briefly review FAR in Subsection II-A. Then, we detail the proposed WMAR in Subsection II-B, and present the resulting radar signal model in Subsection II-C.

A. Preliminaries of FAR

FAR [1] is a technique for enhancing the ECCM and EMC performance of radar systems by using randomized carrier frequencies. In the following we consider a radar system equipped with L antenna elements, uniformly located on an antenna array with distance d between two adjacent elements. Let N be the number of radar pulses transmitted in each coherent processing interval (CPI). Radar pulses are repeatedly transmitted, starting from time instance nT_r to $nT_r + T_p$, $n \in \mathcal{N} := \{0, 1, \dots, N-1\}$, where T_r and T_p represent the pulse repetition interval and pulse duration, respectively, and $T_r > T_p$. Let \mathcal{F} be the set of available carrier frequencies, given by $\mathcal{F} := \{f_c + m\Delta f | m \in \mathcal{M}\}$, where f_c is the initial carrier frequency, $\mathcal{M} := \{0, 1, \dots, M-1\}$, M is the number of available frequencies, and Δf is the frequency step.

In the n -th radar pulse, FAR randomly selects a carrier frequency f_n from \mathcal{F} . The waveform sent from each antenna for the n -th pulse at time instance t is $\phi(f_n, t - nT_r)$, where

$$\phi(f, t) := \text{rect}(t/T_p) e^{j2\pi ft}, \quad (1)$$

and $\text{rect}(t) = 1$ for $t \in [0, 1)$ and zero otherwise, representing rectangular envelope baseband signals.

In order to direct the antenna beam pointing towards a desired angle θ , the signal transmitted by each antenna is weighted by a phase shift $w_l(\theta, f_n) \in \mathbb{C}$ [21], given by

$$w_l(\theta, f) := e^{j2\pi f l d \sin \theta / c}, \quad (2)$$

where c denotes the speed of light. Define the vector $\mathbf{w}(\theta, f) \in \mathbb{C}^L$ whose l -th entry is $[\mathbf{w}(\theta, f)]_l := w_l(\theta, f)$. The transmitted signal can be written as

$$\mathbf{x}_F(n, t) := \mathbf{w}(\theta, f_n) \phi(f_n, t - nT_r). \quad (3)$$

The vector $\mathbf{x}_F(n, t) \in \mathbb{C}^L$ in (3) denotes the transmission vector of the full array for the n -th pulse at time instance t .

The fact that FAR transmits monotone waveform facilitates its cost and hardware requirements. Furthermore, the frequency agility achieved by randomizing the frequencies between pulses enhances survivability in complex electromagnetic environments. However, this comes at the cost of reduced number of radar measurements, which degrades the target recovery performance, particularly in the presence of interference, where some of the radar returns are missed [8]. To overcome these drawbacks, in the following we propose WMAR, which extends FAR to multi-carrier transmissions.

B. WMAR Transmit Signal Model

WMAR extends FAR to multi-carrier signalling. Broadly speaking, WMAR transmits a single multiband waveform from all its antennas, maintaining frequency agility by randomizing a *subset* of the available frequencies on each pulse.

Specifically, in the n -th radar pulse, WMAR randomly selects a set of carrier frequencies \mathcal{F}_n from \mathcal{F} , $\mathcal{F}_n \subset \mathcal{F}$. We assume that the cardinality of \mathcal{F}_n is constant, i.e., $|\mathcal{F}_n| = K$ for each $n \in \mathcal{N}$, and write the elements of this set as $\mathcal{F}_n = \{\Omega_{n,k} | k \in \mathcal{K}\}$, $\mathcal{K} := \{0, 1, \dots, K-1\}$. The portion of the n -th pulse of WMAR in the k -th frequency is given by $\mathbf{x}_{W,k}(n, t) := \frac{1}{\sqrt{K}} \mathbf{w}(\theta, \Omega_{n,k}) \phi(\Omega_{n,k}, t - nT_r)$, and the overall transmitted vector is $\mathbf{x}_W(n, t) = \sum_{k=1}^K \mathbf{x}_{W,k}(n, t)$, i.e.,

$$\mathbf{x}_W(n, t) = \sum_{k=1}^K \frac{1}{\sqrt{K}} \mathbf{w}(\theta, \Omega_{n,k}) \phi(\Omega_{n,k}, t - nT_r), \quad (4)$$

where the factor $\frac{1}{\sqrt{K}}$ guarantees that (4) has the same total power as the FAR signal (3).

FAR is a special case of WMAR under the setting $K = 1$. By using multiple carriers simultaneously via wideband signalling, i.e., $K > 1$, WMAR transmits a highly directional beam, while improving the robustness to missed pulses compared to FAR. The improved performance stems from the use of multi-carrier transmission, which increases the number of radar measurements. To see this, we detail the received signal model of WMAR in the following subsection.

C. WMAR Received Signal Model

We next model the received signal processed by WMAR for target identification. To that aim, we focus on the time interval after the n -th pulse is transmitted, i.e., $nT_r + T_p < t < (n+1)T_r$. In this period, the radar receives echoes of the pulse, which are sampled and processed in discrete-time.

To formulate the radar returns, we assume an ideal scattering point with scattering coefficient $\beta \in \mathbb{C}$ located in the transmit beam of the radar with direction angle ϑ , i.e., $\vartheta \approx \theta$. Denote by $r(t)$ the range between the target and the first radar antenna array element at time t . The scattering point is moving at a constant velocity v radially along with the radar line of sight, i.e., $r(t) = r(0) + vt$. Under the “stop and hop” assumption [22], which assumes that the target hops to a new location when the radar transmits a pulse and stays there until another pulse is emitted, the range in the n -pulse is approximated as

$$r(t) \approx r(nT_r) = r(0) + v \cdot nT_r, \quad nT_r < t < (n+1)T_r. \quad (5)$$

To model the received signal, we first consider the n -th radar pulse that reaches the target, denoted by $\tilde{x}(n, t)$. Let

$\tilde{x}_k(n, t)$ be its component at frequency $\Omega_{n,k}$, i.e., $\tilde{x}(n, t) := \sum_{k=0}^{K-1} \tilde{x}_k(n, t)$. Note that $\tilde{x}_k(n, t)$ is a summation of delayed transmissions from the corresponding antenna elements. The delay for the l -th array element is $r(nT_r)/c + ld \sin \vartheta/c$. Under the narrowband, far-field assumption, using (2), we have that

$$\begin{aligned} \tilde{x}_k(n, t) &= \sum_{l=0}^{L-1} [\mathbf{x}_{W,k}(n, t - r(nT_r)/c)]_l e^{-j2\pi\Omega_{n,k}ld\sin\vartheta/c} \\ &= \mathbf{w}^H(\vartheta, \Omega_{n,k}) \mathbf{x}_{W,k}(n, t - r(nT_r)/c). \end{aligned} \quad (6)$$

Substituting (5) and the definition of $\mathbf{x}_{W,k}(n, t)$ into (6) yields

$$\tilde{x}_k(n, t) = \frac{\rho_W(n, k, \delta_\vartheta)}{\sqrt{K}} \phi\left(\Omega_{n,k}, t - nT_r - \frac{r(0) + nvT_r}{c}\right), \quad (7)$$

where $\delta_\vartheta := \sin \vartheta - \sin \theta$ is the relative direction sine with respect to the transmit beam, and $\rho_W(n, k, \delta_\vartheta) := \mathbf{w}^H(\vartheta, \Omega_{n,k}) \mathbf{w}(\theta, \Omega_{n,k})$ is the transmit gain, expressed as

$$\rho_W(n, k, \delta_\vartheta) = \sum_{l=0}^{L-1} e^{-j2\pi\Omega_{n,k}ld\delta_\vartheta/c}. \quad (8)$$

Note that $\rho_W(n, k, \delta_\vartheta)$ approaches L when $\delta_\vartheta \approx 0$.

Having modeled the signal which reaches the target, we now derive the radar returns observed by the antenna array. After being reflected by the scattering point, the signal at the k -th frequency propagates back to the l -th radar array element with an extra delay of $r(nT_r)/c + ld \sin \vartheta/c$, resulting in

$$[\tilde{y}_{W,k}(n, t)]_l := \beta \tilde{x}_k(n, t - r(nT_r)/c - ld \sin \vartheta/c). \quad (9)$$

The echoes vector $\tilde{\mathbf{y}}_{W,k}(n, t) \in \mathbb{C}^L$ can be written as

$$\begin{aligned} \tilde{\mathbf{y}}_{W,k}(n, t) &= \beta \mathbf{w}^*(\vartheta, \Omega_{n,k}) \tilde{x}_k(n, t - r(nT_r)/c) \\ &\stackrel{(a)}{=} \frac{\beta}{\sqrt{K}} \mathbf{w}^*(\vartheta, \Omega_{n,k}) \rho_W(n, k, \delta_\vartheta) \\ &\quad \times \phi(\Omega_{n,k}, t - nT_r - (2r(0) + 2nvT_r)/c), \end{aligned} \quad (10)$$

where (a) follows from (7).

The received echoes at all K frequencies are then separated and sampled independently by each array element. The signal $\tilde{\mathbf{y}}_{W,k}(n, t)$ is sampled with a rate of $f_s = 1/T_p$ at time instants $t = nT_r + i/f_s$, $i = 0, 1, \dots, \lfloor T_p f_s \rfloor - 1$, such that each pulse is sampled once. Every sample time instant corresponds to a coarse range cell (CRC), $r \in \left(\frac{i-1}{2f_s}c, \frac{i}{2f_s}c\right)$. The division to CRCs indicates coarse range information of scattering points. We focus on an arbitrary i -th CRC, assuming that the scattering point does not move between CRCs during a CPI, i.e., there exists some integer i such that

$$\begin{cases} \frac{i-1}{2f_s}c < r(0) < \frac{i}{2f_s}c, \\ \frac{i-1}{2f_s}c < r(0) + nvT_r < \frac{i}{2f_s}c, \end{cases} \quad \forall n \in \mathcal{N}. \quad (11)$$

Collecting radar returns from N pulses and L elements at the same CRC yields a data cube $\mathbf{Y}_W \in \mathbb{C}^{L \times N \times K}$ with entries

$$[\mathbf{Y}_W]_{l,n,k} := [\tilde{\mathbf{y}}_{W,k}(n, nT_r + i/f_s)]_l, \quad (12)$$

where i is the CRC index. The data cube \mathbf{Y}_W is processed to estimate the refined range information, Doppler, and angle of the scattering point. Data cubes from different CRCs are processed identically and separately.

Finally, we formulate how the unknown parameters of the targets are embedded in the processed data cube \mathbf{Y}_W . To that aim, define $\delta_r := r(0) - ic/2f_s$ as the high-range resolution distance, $c_{n,k} := (\Omega_{n,k} - f_c)/\Delta f \in \mathcal{M}$ as the carrier frequency index, and $\zeta_{n,k} = \Omega_{n,k}/f_c$ as the relative frequency factor. Then, denoting by $\tilde{\beta} := \beta e^{-j4\pi f_c \delta_r/c}$, $\tilde{r} := -4\pi\Delta f \delta_r/c$ and $\tilde{v} := -4\pi f_c v T_r/c$ the generalized scattering intensity, and the normalized range and velocity, respectively, and substituting (10) into (12), we have that

$$[\mathbf{Y}_W]_{l,n,k} = \frac{\tilde{\beta} e^{j\tilde{r}c_{n,k}}}{\sqrt{K}} e^{j\tilde{v}n\zeta_{n,k}} e^{-j2\pi \frac{\Omega_{n,k}l\sin\vartheta}{c}} \rho_W(n, k, \delta_\vartheta). \quad (13)$$

The unknown parameters in (13) are $\tilde{\beta}$, \tilde{r} , \tilde{v} and $(\sin\vartheta, \delta_\vartheta)$, which are used to reveal the scattering intensity $|\beta|$, HRR range $r(0)$, velocity v and angle ϑ of the target.

The above model can be naturally extended to noisy multiple scatterers. When there are S scattering points inside the CRC instead of a single one as assumed previously, the received signal is a summation of returns from all these points corrupted by additive noise, denoted by $\mathbf{N} \in \mathbb{C}^{L \times N \times K}$. Following (13), the entries of the data matrix are

$$[\mathbf{Y}_W]_{l,n,k} = \frac{1}{\sqrt{K}} \sum_{s=0}^{S-1} \tilde{\beta}_s e^{j\tilde{r}_s c_{n,k}} e^{j\tilde{v}_s n \zeta_{n,k}} e^{-j2\pi \Omega_{n,k} l \sin\vartheta_s / c} \times \rho_W(n, k, \delta_{\vartheta_s}) + [\mathbf{N}]_{l,n,k}, \quad (14)$$

where $\{\tilde{\beta}_s\}$, $\{\tilde{r}_s\}$, $\{\tilde{v}_s\}$ and $\{\vartheta_s\}$ represent the sets of factors of scattering coefficients, ranges, velocities, and angles of the S scattering points, respectively, which are unknown and should be estimated. A method for recovering these parameters from the data cube \mathbf{Y}_W is detailed in Section IV.

WMAR has several notable advantages: First, as an extension of FAR, it preserves its frequency agility and is completely suitable for implementation with phased array antennas. Furthermore, as we discuss in Section V, its number of radar measurements for each CRC is increased by a factor of K compared to FAR, thus yielding increased robustness to interference. However, WMAR transmitters simultaneously send multiple carriers instead of a monotone as in FAR, which requires costly hardware with large instantaneous bandwidth, leading to envelope fluctuation and low amplifier efficiency. To overcome these issues, we introduce CAESAR in the following section, which utilizes low complexity narrowband radar transceivers while introducing spatial agility, enabling multi-carrier transmission using monotone signals at a cost of a minimal array antenna gain loss.

III. CAESAR

CAESAR, similarly to WMAR, extends FAR to multi-carrier transmission. However, unlike WMAR, CAESAR utilizes monotone signalling and reception, and is thus more suitable for implementation with reduced cost and low complexity hardware. We detail the transmit and receive models of CAESAR in Subsections III-A and III-B, respectively.

A. CAESAR Transmit Signal Model

Broadly speaking, CAESAR extends FAR to multi-carrier signalling by transmitting monotone waveforms with varying frequencies from different antenna elements. The selection of

the frequencies, as well as their allocation among the antenna elements, is randomized anew in each pulse, thus inducing both *frequency and spatial agility*.

To formulate CAESAR, we consider the same pulse radar formulation detailed in Section II. Similarly to WMAR detailed in Subsection II-B, in the n -th radar pulse, CAESAR randomly selects a set of carrier frequencies $\mathcal{F}_n = \{\Omega_{n,k} | k \in \mathcal{K}\}$ from \mathcal{F} . While WMAR uses the set of selected frequencies to generate wideband waveforms, CAESAR allocates a sub-array for each frequency, such that all the antenna array elements are utilized for transmission, each at a single carrier frequency. Denote by $f_{n,l} \in \mathcal{F}_n$ the frequency used by the l -th antenna array element, $l \in \mathcal{L} := \{0, 1, \dots, L-1\}$. After phase shifting the waveform to direct the beam, the l -th array element transmission can be written as

$$[\mathbf{x}_C(n, t)]_l := [\mathbf{w}(\theta, f_{n,l})]_l \phi(f_{n,l}, t - nT_r). \quad (15)$$

The vector $\mathbf{x}_C(n, t) \in \mathbb{C}^L$ in (15) denotes the full array transmission vector for the n -th pulse at time t . Here, unlike FAR which transmits a single frequency from the full array (3), CAESAR assigns diverse frequencies to different sub-array antennas, as illustrated in Fig. 1.

The transmitted signal (15) can also be expressed by grouping the array elements which use the same frequency $\Omega_{n,k}$. Let $\mathbf{x}_{C,k}(n, t) \in \mathbb{C}^L$ with zero padding represent the portion of $\mathbf{x}_C(n, t)$ which utilizes $\Omega_{n,k}$, i.e.,

$$\mathbf{x}_{C,k}(n, t) = \mathbf{P}(n, k) \mathbf{w}(\theta, \Omega_{n,k}) \phi(\Omega_{n,k}, t - nT_r), \quad (16)$$

where $\mathbf{P}(n, k) \in \{0, 1\}^{L \times L}$ is a diagonal selection matrix with diagonal $\mathbf{p}(n, k) \in \{0, 1\}^L$, whose l -th entry is one if the l -th array element transmits at frequency $\Omega_{n,k}$ and zero otherwise, i.e., $[\mathbf{p}(n, k)]_{l,l} = [\mathbf{p}(n, k)]_l = 1$ and $[\mathbf{x}_{C,k}(n, t)]_l = [\mathbf{x}_C(n, t)]_l$ when $f_{n,l} = \Omega_{n,k}$. The transmitted signal is thus $\mathbf{x}_C(n, t) := \sum_{k=0}^{K-1} \mathbf{x}_{C,k}(n, t)$, namely

$$\mathbf{x}_C(n, t) = \sum_{k=0}^{K-1} \mathbf{P}(n, k) \mathbf{w}(\theta, \Omega_{n,k}) \phi(\Omega_{n,k}, t - nT_r). \quad (17)$$

Comparing (17) with (4), we find that each array element of CAESAR transmits a single frequency with unit amplitude while in WMAR all K frequencies with amplitudes scaled by a factor $1/\sqrt{K}$ are sent by each element.

The diagonal selection matrices $\mathbf{P}(n, 0), \dots, \mathbf{P}(n, K-1)$ uniquely describe the allocation of antenna elements for the n -th pulse. CAESAR transmission scheme implies that $\sum_{k=0}^{K-1} \mathbf{P}(n, k) = \mathbf{I}_L$, i.e., all the antenna elements are utilized for the transmission of the n -th pulse. The trace of $\mathbf{P}(n, k)$ represents the number of antennas using the k -th frequency. Without loss of generality, we assume that L/K is an integer and $\text{tr}(\mathbf{P}(n, k)) = L/K$, for each $n \in \mathcal{N}$ and $k \in \mathcal{K}$.

Conventional phased array FAR and FDA [14] are special cases of CAESAR with $K = 1$ and $K = M = L$, respectively. A fundamental difference between these radar schemes is the transmit beam pattern. In FAR, the same carrier frequency is utilized by all the elements, i.e., $\Omega_{n,k}$ and $f_{n,l}$ are identical for each $k \in \mathcal{K}$ and $l \in \mathcal{L}$, respectively, resulting in highly directional beam. In FDA, all available frequencies are transmitted simultaneously and one frequency corresponds to a single antenna element, leading to an omnidirectional

beam which degrades radar performance and is not suitable for target tracking [15]. The proposed CAESAR uses only a subset of the available frequencies in each pulse and multiple antenna elements share the same frequency, thus achieving a compromise radiation beam that only illuminates the desired angle. Despite the gain loss in comparison with FAR discussed in Section V, CAESAR achieves improved range-Doppler reconstruction performance and increased robustness to interference, as numerically demonstrated in Section VII.

B. CAESAR Received Signal Model

We next model the received signal processed by CAESAR. Unlike WMAR, in which each antenna receives and separates different frequency components, in CAESAR, the l -th antenna element only receives radar returns at frequency $f_{n,l}$, and abandons other frequencies. This enables the use of narrowband receivers, simplifying the hardware requirements.

Note that the derivation of the signal component received at the k -th frequency in (6), $\tilde{x}_k(n, t)$, does not depend on the specific radar scheme. Here, substituting (16) into (6) yields

$$\tilde{x}_k(n, t) = \rho_C(n, k, \delta_\vartheta) \phi \left(\Omega_{n,k} t - nT_r - \frac{r(0) + nvT_r}{c} \right), \quad (18)$$

where $\rho_C(n, k, \delta_\vartheta) := \mathbf{w}^H(\vartheta, \Omega_{n,k}) \mathbf{P}(n, k) \mathbf{w}(\theta, \Omega_{n,k})$ is the transmit gain of the selected sub-array antenna, expressed as

$$\rho_C(n, k, \delta_\vartheta) = \sum_{l=0}^{L-1} [\mathbf{p}(n, k)]_l e^{-j2\pi\Omega_{n,k} l d \delta_\vartheta / c}. \quad (19)$$

Note that, opposed to the transmit gain of WMAR in (8) which tends to L , $\rho_C(n, k, \delta_\vartheta)$ approaches L/K when $\delta_\vartheta \approx 0$. By repeating the arguments in the derivation of (10), the echoes vector $\tilde{\mathbf{y}}_{C,k}(n, t) \in \mathbb{C}^L$ can be written as

$$\begin{aligned} \tilde{\mathbf{y}}_{C,k}(n, t) = & \beta \mathbf{w}^*(\vartheta, \Omega_{n,k}) \rho_C(n, k, \delta_\vartheta) \\ & \times \phi(\Omega_{n,k} t - nT_r - (2r(0) + 2nvT_r)/c). \end{aligned} \quad (20)$$

CAESAR receives and processes impinging signals by the corresponding elements of the antenna array. In particular, only a sub-array, whose elements are indicated by $\mathbf{P}(n, k)$, receives the impinging signal $\tilde{\mathbf{y}}_{C,k}(n, t)$; the other array elements are tuned to other frequencies. The zero-padded received signal at the k -th frequency, denoted by $\mathbf{y}_{C,k}(n, t) \in \mathbb{C}^L$, is thus $\mathbf{y}_{C,k}(n, t) := \mathbf{P}(n, k) \tilde{\mathbf{y}}_{C,k}(n, t)$. The full array received signal is given by $\mathbf{y}_C(n, t) := \sum_{k=0}^{K-1} \mathbf{y}_{C,k}(n, t)$.

The observed signal $\mathbf{y}_C(n, t)$ is sampled in a similar manner as detailed in Subsection II-C. Since CAESAR processes a single frequency component per antenna element, the measurements from each CRC are collected together as a data matrix $\mathbf{Y} \in \mathbb{C}^{L \times N}$, as opposed to a $L \times N \times K$ cube processed by WMAR. By repeating the arguments used for obtaining (13), it holds that

$$[\mathbf{Y}]_{l,n} = \tilde{\beta} e^{j\tilde{r}_c c_{n,k}} e^{j\tilde{v}_n \zeta_{n,k}} e^{-j2\pi\Omega_{n,k} l d \sin \vartheta / c} \rho_C(n, k, \delta_\vartheta), \quad (21)$$

which can be extended to account for multiple targets and noisy measurements as in (14), i.e.,

$$\begin{aligned} [\mathbf{Y}]_{l,n} = & \sum_{s=0}^{S-1} \tilde{\beta}_s e^{j\tilde{r}_s c_{n,k}} e^{j\tilde{v}_s n \zeta_{n,k}} e^{-j2\pi\Omega_{n,k} \frac{l d \sin \vartheta_s}{c}} \\ & \times \rho_C(n, k, \delta_{\vartheta_s}) + [\mathbf{N}]_{l,n}, \end{aligned} \quad (22)$$

where $\mathbf{N} \in \mathbb{C}^{L \times N}$ is the additive noise. In order to recover the unknown parameters from the acquired data matrix (22), in the following section we present a dedicated recovery scheme.

IV. TARGET RECOVERY METHOD

Here, we present an algorithm for reconstructing the unknown HRR range, velocity, angle, and scattering intensity parameters of the scattering points from the radar measurements of both WMAR and CAESAR. In order to maintain feasible computational complexity, we do not estimate all these parameters simultaneously: our proposed algorithm first jointly recovers the range-Doppler parameters followed by estimation of the unknown angles. When performing joint range-Doppler estimation, we assume that all the scattering points are located within the mainlobe of the transmit beam, and that the difference of the angle sine is negligible, i.e., $\delta_\vartheta \approx 0$. We then estimate the direction angles of all scattering points based on their range-Doppler estimates.

We divide the target recovery method into three stages: 1) apply receive beamforming such that the magnitude of the received signal is enhanced, facilitating range-Doppler estimation; 2) apply CS methods for joint reconstruction of range and Doppler; and 3) angle and scattering intensity estimation. These steps are discussed in Subsections IV-A-IV-C, respectively. A theoretical analysis of the range-Doppler estimation performance of our algorithm is provided in Section VI, where we quantify how using multiple carriers improves the range-Doppler reconstruction performance.

A. Receive Beamforming

The first step in processing the radar measurements is to beamform the received signal in order to facilitate recovery of the range-Doppler parameters. This receive beamforming is applied to radar returns at different frequencies separately. To formulate the beamforming technique, we henceforth focus on the k -th frequency of the n -th pulse, $\Omega_{n,k}$. For both CAESAR and WMAR, a total of L measurements correspond to $\Omega_{n,k}$, and are denoted $\tilde{\mathbf{z}}_{n,k} \in \mathbb{C}^L$. For CAESAR, $\tilde{\mathbf{z}}_{n,k}$ is given by $\tilde{\mathbf{z}}_{n,k} = \mathbf{P}(n, k) [\mathbf{Y}_C]_n$, of which only elements corresponding to the selected sub-array are nonzero. For WMAR, $\tilde{\mathbf{z}}_{n,k}$ consists of the entries $[\mathbf{Y}_W]_{l,n,k}$ for each $l \in \mathcal{L}$. These measurements are integrated with the weights $\mathbf{w}(\theta, \Omega_{n,k})$ such that the receive beam is pointed towards θ , resulting in

$$Z_{k,n} := \mathbf{w}^T \tilde{\mathbf{z}}_{n,k} \in \mathbb{C}. \quad (23)$$

Define $\alpha_K := L^2/K^2$ for CAESAR, and $\alpha_K := L^2/\sqrt{K}$ for WMAR. When $\delta_{\vartheta_s} \approx 0$, i.e., the beam direction θ is close to the true angle of the target, the resulting beam pattern can be simplified as stated in the following lemma:

Lemma 1. *If the difference of the angle sine satisfies $\delta_{\vartheta_s} \approx 0$, then $Z_{k,n}$ in (23) can be approximated as*

$$Z_{k,n} \approx \alpha_K \sum_{s=0}^{S-1} \tilde{\beta}_s e^{j\tilde{r}_s c_{n,k}} e^{j\tilde{v}_s n \zeta_{n,k}}. \quad (24)$$

Proof. See Appendix A. \square

The receive beamforming produces the matrix $\mathbf{Z} \in \mathbb{C}^{K \times N}$ whose entries are $[\mathbf{Z}]_{k,n} := Z_{k,n}$, for each $k \in \mathcal{K}$, $n \in \mathcal{N}$. Under the approximation (24), the obtained \mathbf{Z} is used for range-Doppler reconstruction, as discussed in the next subsection.

It follows from (24) that the amplitudes of the radar returns of CAESAR are inversely proportional to K^2 , a property which stems from the fact that CAESAR adopts a sub-array to transmit each carrier. This reveals the tradeoff between the number of beamformed observations, KN , and the round-trip antenna gain, $\alpha_K = L^2/K^2$. In particular, Lemma 1 indicates that the selection of K induces some tradeoff between number of beamformed observations and intensity, and that increasing K does not improve the radar performance monotonically. For comparison, WMAR utilizes the same beamformed matrix with intensity increased by a factor of $K^{3/2}$. This indicates that the usage of costly wideband waveforms results in the same number of beamformed observations with increased gain. The resulting tradeoff between number of beamformed observations and their intensity, induced by the selection of K , is not the only aspect which must be accounted for when setting the value of K , as it also affects the frequency agility profile. In particular, smaller K values result in increased spectral flexibility, as different pulses are more likely to use non-overlapping frequency sets. Consequently, in our numerical analysis in Section VII we use small values of K , for which the gain loss between CAESAR and WMAR is less significant, and increased frequency agility is maintained.

B. Range-Doppler Reconstruction

To reconstruct the range-Doppler parameters, we first recast the beamformed signal model of Lemma 1 in matrix form, and then apply CS methods to recover the unknown parameters, exploiting the underlying sparsity of the resulting model.

To obtain a sparse recovery problem, we start by discretizing the range and Doppler domains. Recall that \tilde{r}_s and \tilde{v}_s denote the normalized range and Doppler parameters, with resolutions $\frac{2\pi}{M}$ and $\frac{2\pi}{N}$, corresponding to the numbers of available frequencies and pulses, respectively. Both parameters belong to continuous domains in the unambiguous region $(\tilde{r}_s, \tilde{v}_s) \in [0, 2\pi)^2$. We discretize \tilde{r}_s and \tilde{v}_s into HRR and Doppler grids, denoted by grid sets $\mathcal{R} := \{\frac{2\pi m}{M} \mid m \in \mathcal{M}\}$ and $\mathcal{V} := \{\frac{2\pi n}{N} \mid n \in \mathcal{N}\}$, respectively, and assume that the targets are located precisely on the grids. The target scene can now be represented by the matrix $\mathbf{B} \in \mathbb{C}^{M \times N}$ with entries

$$[\mathbf{B}]_{m,n} := \begin{cases} \tilde{\beta}_s \alpha_K, & \text{if } (\tilde{r}_s, \tilde{v}_s) = \left(\frac{2\pi m}{M}, \frac{2\pi n}{N}\right), \\ 0, & \text{otherwise.} \end{cases} \quad (25)$$

We can now use the sparse structure of (25) to formulate the range-Doppler reconstruction as a sparse recovery problem. To that aim, let $\mathbf{z} \in \mathbb{C}^{KN}$ and $\boldsymbol{\beta} \in \mathbb{C}^{MN}$ be the vectorized representations of \mathbf{Z} and \mathbf{B} , respectively, i.e., $[\mathbf{z}]_{k+nK} = Z_{k,n}$ and $[\boldsymbol{\beta}]_{n+mN} := [\mathbf{B}]_{m,n}$. From (24), it holds that

$$\mathbf{z} = \boldsymbol{\Phi} \boldsymbol{\beta}, \quad (26)$$

where the entries of $\boldsymbol{\Phi} \in \mathbb{C}^{KN \times MN}$ are given by

$$[\boldsymbol{\Phi}]_{k+nK, l+mN} := e^{j\frac{2\pi m}{M} c_{n,k} + j\frac{2\pi l}{N} n \zeta_{n,k}}, \quad (27)$$

$m \in \mathcal{M}$, $l, n \in \mathcal{N}$, and $k \in \mathcal{K}$. The matrix $\boldsymbol{\Phi}$ is determined by the frequencies utilized in each pulse. Consequently, $\boldsymbol{\Phi}$ is a random matrix, as these parameters are randomized by the radar transmitters, whose realization is known to the receiver.

In the presence of noisy radar returns, (26) becomes

$$\mathbf{z} = \boldsymbol{\Phi} \boldsymbol{\beta} + \mathbf{n}, \quad (28)$$

where the entries of the noise vector $\mathbf{n} \in \mathbb{C}^{KN}$ are the beamformed noise, e.g., for CAESAR these are given by $[\mathbf{n}]_{k+nK} = \mathbf{w}^T(\theta, \Omega_{n,k}) \mathbf{P}(n, k) [N]_n$.

Since in each pulse only a subset of the available frequencies are transmitted, i.e., $K \leq M$, the sensing matrix $\boldsymbol{\Phi}$ in (28) has more columns than rows, $MN \geq KN$, indicating that solving (28) is naturally an under-determined problem. When $\boldsymbol{\beta}$ is S -sparse, which means that there are S non-zeroes in $\boldsymbol{\beta}$, and $S \ll MN$, CS algorithms can be used to solve (28), and the range-Doppler parameters of the targets may then be recovered from the support set of $\boldsymbol{\beta}$, denoted $\mathcal{S} := \{s \mid [\boldsymbol{\beta}]_s \neq 0\}$. With the recovered range-Doppler values, the angle and scattering intensity are estimated as detailed in the following subsection.

C. Angle and Scattering Intensity Estimation

In this part, we refine the angle estimation of the scattering points, which are coarsely assumed within the transmit beam in the receive beamforming step, i.e., $\delta_\vartheta \approx 0$. While the following formulation focuses on CAESAR, the resulting algorithm is also applicable for WMAR as well as FAR.

We estimate the directions of the scatterers individually, as different points may have different direction angles. Since after receive beamforming some directional information is lost in \mathbf{Z} , we recover the angles from the original data matrix \mathbf{Y}_C (22). Using the obtained range and Doppler estimates, we first isolate echoes for each scattering point with an orthogonal projection, and apply a matched filter to estimate the direction angle of each scattering point. Finally, we use least squares to infer the scattering intensities.

1) *Echo isolation using orthogonal projection:* In order to accurately estimate the angle of each scattering point, it is necessary to mitigate the interference between scattering points. To that aim, we use an orthogonal projection to isolate echoes from each scattering point.

Let $\widehat{\mathcal{S}}$ be the support set of $\widehat{\boldsymbol{\beta}}$, the estimate of $\boldsymbol{\beta}$, and infer the normalized range and Doppler parameters $\{\tilde{r}_s, \tilde{v}_s\}$ from $\widehat{\mathcal{S}}$. According to (22), given these parameters, the original data vector from the l -th array element can be written as

$$[\mathbf{Y}_C^T]_l = [\boldsymbol{\Psi}_l]_{\widehat{\mathcal{S}}} [\gamma_l]_{\widehat{\mathcal{S}}} + [\mathbf{N}^T]_l, \quad (29)$$

where $\boldsymbol{\Psi}_l \in \mathbb{C}^{N \times MN}$ has entries $[\boldsymbol{\Psi}_l]_{n,s} := e^{j\tilde{r}_s c_{n,k} + j\tilde{v}_s n \zeta_{n,k}}$, and $\gamma_l \in \mathbb{C}^{MN}$ denotes the effective scattering intensities corresponding to all discrete range-Doppler grids, with s -th entry $[\gamma_l]_s := \tilde{\beta}_s \rho(n, k, \delta_\vartheta) e^{-j2\pi \Omega_{n,k} l d \sin \vartheta_s / c}$. The intensities, containing unknown phase shifts and antenna gains due to angles ϑ_s , are estimated as

$$[\hat{\gamma}_l]_{\widehat{\mathcal{S}}} = \arg \min_{[\gamma_l]_{\widehat{\mathcal{S}}}} \|[\mathbf{Y}_C^T]_l - [\boldsymbol{\Psi}]_{\widehat{\mathcal{S}}} [\gamma_l]_{\widehat{\mathcal{S}}}\|_2^2 = [\boldsymbol{\Psi}]_{\widehat{\mathcal{S}}}^\dagger [\mathbf{Y}_C^T]_l,$$

where $\mathbf{A}^\dagger = (\mathbf{A}^H \mathbf{A})^{-1} \mathbf{A}^H$ and we assume that $|\widehat{\mathcal{S}}| < N$ and $\mathbf{A}^H \mathbf{A}$ is invertible. The received radar echo from the s -th scattering point, $\widehat{\mathbf{Y}}_s \in \mathbb{C}^{L \times N}$, $s \in \widehat{\mathcal{S}}$, is then reconstructed by setting the l -th row as

$$[\widehat{\mathbf{Y}}_s^T]_l = [\boldsymbol{\Psi}]_s [\hat{\gamma}_l]_s. \quad (30)$$

2) *Angle estimation using matched filter:* With the isolated echoes $\hat{\mathbf{Y}}_s$ of the s -th scattering point, we use a matched filter to refine the unknown angle ϑ_s , which is coarsely assumed within the beam in the previous receive beamforming procedure, i.e., $\vartheta_s \in \Theta := \theta + [-\frac{\pi}{2L}, \frac{\pi}{2L}]$. Using (22), we write the isolated echo as $\hat{\mathbf{Y}}_s = \tilde{\beta}_s \mathbf{Y}_s(\vartheta_s) + \mathbf{N}_s$, where \mathbf{N}_s denotes the noise matrix corresponding to the s -th scattering point. The entries of the steering matrix $\mathbf{Y}_s(\vartheta_s) \in \mathbb{C}^{L \times N}$ are

$$[\mathbf{Y}_s(\vartheta_s)]_{l,n} := \rho_C(n, k, \delta_{\vartheta_s}) e^{j\tilde{r}_s c_{n,k}} e^{j\tilde{v}_s n \zeta_{n,k}} e^{-j2\pi \Omega_{n,k} l d \sin \vartheta_s / c},$$

which can be computed using (19) with given ϑ_s and the estimates of the range-Doppler parameters. Note that $\tilde{\beta}_s$, ϑ_s and \mathbf{N}_s are unknown, and ϑ_s is of interest. The value of the intensity $\tilde{\beta}_s$ recovered next is refined in the sequel to improve accuracy. Here, we apply least squares estimation, i.e.,

$$\hat{\vartheta}_s, \hat{\tilde{\beta}}_s = \arg \min_{\vartheta_s, \tilde{\beta}_s} \|\text{vec}(\hat{\mathbf{Y}}_s) - \tilde{\beta}_s \text{vec}(\mathbf{Y}_s(\vartheta_s))\|_2^2. \quad (31)$$

Substituting $\hat{\tilde{\beta}}_s = (\text{vec}(\mathbf{Y}_s(\vartheta_s)))^\dagger \text{vec}(\hat{\mathbf{Y}}_s) = \frac{\text{tr}(\mathbf{Y}_s^H(\vartheta_s) \hat{\mathbf{Y}}_s)}{\|\mathbf{Y}_s(\vartheta_s)\|_F^2}$ into (31) yields a matched filter

$$\hat{\vartheta}_s = \arg \max_{\vartheta_s \in \Theta} \frac{|\text{tr}(\mathbf{Y}_s^H(\vartheta_s) \hat{\mathbf{Y}}_s)|^2}{\|\mathbf{Y}_s(\vartheta_s)\|_F^2}. \quad (32)$$

The angle $\hat{\vartheta}_s$ is estimated for each $s \in \hat{\mathcal{S}}$ via (32) separately.

3) *Scattering intensity estimation using least squares:* When $\delta_{\vartheta_s} \neq 0$, there exist approximation errors in (24) and the resultant intensity estimate $\hat{\beta}$. We thus propose to refine the estimation of β from the original data matrix \mathbf{Y}_C once the range-Doppler and angle parameters are acquired. Given estimated angles $\hat{\vartheta}_s$, we concatenate the steering vectors into

$$\mathbf{C} := \left[\text{vec}(\mathbf{Y}_{s_0}(\hat{\vartheta}_{s_0})), \text{vec}(\mathbf{Y}_{s_1}(\hat{\vartheta}_{s_1})), \dots \right],$$

$s_0, s_1, \dots \in \hat{\mathcal{S}}$. The model (22) is rewritten as $\text{vec}(\mathbf{Y}_C) = \mathbf{C}[\beta]_{\hat{\mathcal{S}}} + \mathbf{N}$, and β can be re-estimated via least squares as

$$[\hat{\beta}]_{\hat{\mathcal{S}}} = \arg \min_{[\beta]_{\hat{\mathcal{S}}}} \|\text{vec}(\mathbf{Y}_C) - \mathbf{C}[\beta]_{\hat{\mathcal{S}}}\|_2^2 = \mathbf{C}^\dagger \text{vec}(\mathbf{Y}_C). \quad (33)$$

The overall recovery method is summarized as Algorithm 1.

Algorithm 1 CAESAR target recovery

- 1: Input: Data matrix \mathbf{Y}_C .
- 2: Beamform \mathbf{Y}_C into \mathbf{Z} via (23).
- 3: Use CS methods to recover the support of β , denoted by $\hat{\mathcal{S}}$, from \mathbf{Z} based on the sensing matrix Φ (27).
- 4: Reconstruct the normalized range-Doppler parameters $\{\tilde{r}_s, \tilde{v}_s\}$ from $\hat{\mathcal{S}}$ based on (25).
- 5: Isolate \mathbf{Y}_C into multiple echoes $\{\hat{\mathbf{Y}}_s\}$ via (30).
- 6: Recover the angles $\{\vartheta_s\}$ from $\{\hat{\mathbf{Y}}_s\}$ via (32).
- 7: Refine the scattering intensities $\{\beta_s\}$ using (33).
- 8: Output: parameters $\{\tilde{r}_s, \tilde{v}_s, \vartheta_s, \beta_s\}$.

V. COMPARISON TO RELATED RADAR SCHEMES

We next compare our proposed WMAR and CAESAR schemes, and discuss their relationship with relevant previously proposed radar methods.

A. Comparison of WMAR, CAESAR, and FAR

We compare our proposed schemes to each other, as well as to FAR, which is a special case of both WMAR and CAESAR obtained by setting $K = 1$. We focus on the following aspects: 1) system complexity; 2) the number of measurements in a CPI; and 3) amplitudes of the received signals. A numerical comparison of the target recovery performance of the considered radar schemes is provided in Section VII.

In terms of system complexity, recall that CAESAR and FAR use narrowband transceivers, and only a monotone signal is transmitted or received by each element. In WMAR, K multi-tone signals are sent and received simultaneously in each pulse, thus it requires instantaneous wideband components, resulting in a more complex system structure.

To compare the number of obtained measurements, we note that for each CPI, WMAR acquires a data cube with NLK samples, while FAR and CAESAR collect NL samples in the data matrix. After receive beamforming, the number of observations become N , NK and NK , for FAR, CAESAR, and WMAR, respectively, via (23). This indicates that the multi-carrier waveforms of CAESAR and WMAR increase the number of measurements after receive beamforming.

The amplitudes of the received signals are also different, as the transmitted power and antenna gains differ. Assuming average per-antenna unit power, in FAR, all L array elements transmit at the single selected frequency, and the total power is L . The corresponding power for each frequency component of CAESAR and WMAR is L/K . Additionally, FAR and WMAR use a full array for the selected frequency. Hence, they have higher antenna gains than CAESAR that uses a subset of the antenna array for each carrier. When we consider a scattering point with unit intensity and $\delta_{\vartheta} \approx 0$, it follows from Lemma 1 that the amplitudes of the received signals after receive beamforming, denoted α_K , are L^2 and L^2/\sqrt{K} for FAR and WMAR, respectively, while the corresponding amplitude of CAESAR is L^2/K^2 . This amplitude reduction can affect the performance of CAESAR in the presence of noise, as demonstrated in the numerical study in Section VII.

The above comparison reveals the tradeoff between system complexity, number of observations, and signal amplitudes. Among these three factors, the number of observations is crucial to the target recovery performance especially in complex electromagnetic environments, where some observations may be discarded due to strong interference [9], [10]. The proposed multi-carrier schemes, WMAR and CAESAR, are numerically shown to outperform FAR in Section VII, despite the gain loss of CAESAR. CAESAR also achieves performance within a relatively small gap compared to the costly WMAR, while avoiding the hardware complexity associated with the usage of instantaneous wideband components. In addition, CAESAR can also exploit its spatial agility character, which is not present in FAR or WMAR, to realize a DFRC system, as discussed in our companion paper [20].

B. Comparison to Previously Proposed Schemes

Similarly to CAESAR, previously proposed FDMA-MIMO radar [11], SUMMeR [12], and FDA radar [13], [14] schemes

also transmit a monotone waveform from each antenna element while different elements simultaneously transmit multiple carrier frequencies. The main differences between our approaches and these previous methods are beam pattern, frequency agility, and system complexity. Due to the transmission of diverse carrier frequencies from different array elements of FDMA-MIMO/SUMMeR/FDA, the array antenna does not form a focused transmit beam and usually illuminates a large field-of-view [15]. This results in a transmit gain loss which degrades the performance, especially for track mode, where a high-gain directional beam is preferred [15]. By transmitting each selected frequency with an antenna array (the full array in WMAR and a sub-array in CAESAR), our methods achieve a focused beam pattern that facilitates accurate target recovery.

Furthermore, FDMA-MIMO and FDA transmit all available frequencies simultaneously, and thus do not share the advantages of frequency agility, e.g., improved ECCM and EMC performance, as the multi-carrier version of SUMMeR and the proposed WMAR/CAESAR. In addition, FDMA-MIMO, SUMMeR and WMAR receive instantaneous wideband signals with every single antenna, requiring more costly components than FDA [14] and CAESAR, which use narrowband receivers.

To summarize, unlike previously proposed radar methods, our proposed schemes are based on phased array antenna and frequency agile waveforms to achieve directional transmit beam and high resistance against interference. In terms of complexity, CAESAR is preferred for its usage of monotone waveforms and simple instantaneous narrowband receiver.

VI. RANGE-DOPPLER RECONSTRUCTION ANALYSIS

Range-Doppler reconstruction plays a crucial role in target recovery. This section presents a theoretical analysis of range-Doppler recovery of Algorithm 1. Since both WMAR and CAESAR are generalizations of FAR, the following analysis is inspired by the study of CS-based FAR recovery in [7]. In particular, we extend the results of [7] to multi-carrier waveforms, as well as to extremely complex electromagnetic environments, where some transmitted pulses are interfered by intentional or unintentional interference. In the presence of such interference, only partial observations in the beamformed matrix Z remain effective for range-Doppler reconstruction. As mentioned in Subsection IV-B, Algorithm 1 utilizes CS algorithms to recover the range-Doppler parameters. Accordingly, our performance study is based on CS theory. To present the analysis, we first briefly review some basic concepts of CS in Subsection VI-A, followed by the range-Doppler recovery performance analysis in Subsection VI-B. .

A. Review of Compressed Sensing

CS methods aim to solve under-determined problems such as (26) by seeking the sparsest solution, i.e.,

$$\min_{\beta} \|\beta\|_0, \text{ s.t. } z = \Phi\beta. \quad (34)$$

The ℓ_0 optimization in (34) is generally NP-hard. To reduce computational complexity, many alternatives including ℓ_1 optimization and greedy approaches have been suggested to approximate (34), see [23], [24].

There have been extensive studies on theoretical conditions that guarantee unique recovery for noiseless models or robust

recovery for noisy models [23], [24]. The majority of these studies characterize conditions and properties of the measurement matrix Φ , including spark, mutual incoherence property (MIP) and restricted isometry property (RIP).

Following [7], we focus on the MIP. A sensing matrix Φ is said to satisfy the MIP when its coherence, defined as

$$\mu(\Phi) := \max_{i \neq j} \frac{|\langle \Phi_i^H, \Phi_j \rangle|}{\|\Phi_i\|_2 \|\Phi_j\|_2}, \quad (35)$$

is not larger than some predefined threshold. Bounded coherence ensures unique or robust recovery using a variety of computationally efficient CS methods. We take ℓ_1 optimization as an example to explain the bounds on matrix coherence. In the absence of noise, the basis pursuit algorithm solves

$$\min_{\beta} \|\beta\|_1, \text{ s.t. } z = \Phi\beta, \quad (36)$$

instead of (34). The uniqueness of the solution to (36) is guaranteed by the following theorem:

Theorem 2 ([25]). *Suppose the sensing matrix Φ has coherence $\mu(\Phi) < \frac{1}{2S-1}$. If β solves (36) and has support size S , then β is the unique solution to (36).*

Based on Theorem 2, we next analyze the coherence measure of the sensing matrix Φ in (27) for CAESAR and WMAR (whose sensing matrices are identical), and establish the corresponding performance guarantees.

B. Performance Analysis

Here, we analyze the range-Doppler reconstruction of WMAR and CAESAR. Since the sensing matrix Φ is random, we start by analyzing its statistics, and then derive conditions that ensure unique recovery by invoking Theorem 2.

We assume that the frequency set \mathcal{F}_n is uniformly i.i.d. over $\{\mathcal{X} | \mathcal{X} \subset \mathcal{F}, |\mathcal{X}| = K\}$. For mathematical convenience, in our analysis we adopt the narrow relative bandwidth assumption from [7], i.e., $\zeta_{n,k} \approx 1$, such that (27) becomes

$$[\Phi]_{k+nK, l+mN} = e^{j \frac{2\pi m}{M} c_{n,k} + j \frac{2\pi l}{N} n}. \quad (37)$$

Numerical results in [7] indicate that large relative bandwidth has negligible effect on the MIP of Φ . In addition, recall that all the targets precisely lie on the predefined grid points, as assumed in Subsection IV-B.

In complex electromagnetic environments, some of the radar echoes may be corrupted due to jamming or interference. Heavily corrupted echoes are unwanted and should be removed before processing in order to avoid their influence on the estimation of target parameters [9], [10]. In this case, the corrupted radar returns are identified, as such echoes typically have distinct characters, e.g., extremely large amplitudes. These interfered observations are regarded as missing, where we consider two kinds of missing patterns: 1) pulse selective, i.e., all observations in certain pulses are missing, which happens when the interference in these pulses is intense over all sub-bands; 2) observation selective, namely, only parts of the observations are missed when the corresponding pulse is interfered. We consider the first case in this subsection, assuming that the radar receiver knows which pulses are

corrupted, and leave the analysis under the second case for future investigation. In particular, we adopt the missing-or-not approach [26], in which each pulse in z has a probability of $1 - u$, $0 < u < 1$, to be corrupted, and the missing-or-not status of the pulses are statistically independent of each other.

After removing the corrupted returns, only part of the observations in the beamformed vector z (28) are used for range-Doppler recovery. Equivalently, corresponding rows in Φ can be regarded as missing, affecting the coherence of the matrix and thus the reconstruction performance. Denote by $\Lambda \subset \mathcal{N}$ the random set of available pulse indexes and by $\Lambda_* := \{nK + k \mid n \in \Lambda, k \in \mathcal{K}\}$ the corresponding index set of available observations. The signal model (28) is now

$$z_* = \Phi_* \beta + n_*, \quad (38)$$

where $z_* := [z]_{\Lambda_*}$, $\Phi_* := [\Phi^T]_{\Lambda_*}^T$, and $n_* := [n]_{\Lambda_*}$.

Consider the inner product of two columns in Φ_* , denoted $[\Phi_*]_{l_1}$ and $[\Phi_*]_{l_2}$, corresponding to grid points $(\frac{2\pi m_1}{M}, \frac{2\pi n_1}{N})$ and $(\frac{2\pi m_2}{M}, \frac{2\pi n_2}{N})$, respectively, $l_1, l_2 \in 0, 1, \dots, MN - 1$, $m_1, m_2 \in \mathcal{M}$, $n_1, n_2 \in \mathcal{N}$. While there are $M^2 N^2$ different pairs of (l_1, l_2) , the magnitude of the inner product $|\Phi_*|_{l_1}^H [\Phi_*]_{l_2}|$, which determines the coherence of Φ_* , takes at most $MN - 1$ distinct random values. To see this, note that

$$\begin{aligned} [\Phi_*]_{l_1}^H [\Phi_*]_{l_2} &= \sum_{n \in \Lambda} \sum_{k=0}^{K-1} e^{-j \frac{2\pi m_1}{M} c_{n,k} - j \frac{2\pi n_1}{N} n} e^{j \frac{2\pi m_2}{M} c_{n,k} + j \frac{2\pi n_2}{N} n} \\ &= \sum_{n \in \Lambda} \sum_{k=0}^{K-1} e^{-j 2\pi \frac{m_1 - m_2}{M} c_{n,k} - j 2\pi \frac{n_1 - n_2}{N} n}, \end{aligned} \quad (39)$$

indicating that the inner product depends only on the difference of the grid points, i.e., $m_1 - m_2$ and $n_1 - n_2$, and not on the individual values of the column indices l_1 and l_2 . It follows from (39) that the MIP of Φ_* can be written as

$$\mu(\Phi_*) = \max_{\substack{(\Delta_m, \Delta_n) \\ \neq (0,0)}} \frac{1}{|\Lambda|K} \sum_{n \in \Lambda} \sum_{k=0}^{K-1} e^{-j \Delta_m c_{n,k} - j \Delta_n n}. \quad (40)$$

where $\Delta_m := 2\pi \frac{m_1 - m_2}{M}$, $\Delta_n := 2\pi \frac{n_1 - n_2}{N}$ take values in the sets $\Delta_m \in \{\pm \frac{2\pi m}{M}\}_{m \in \mathcal{M}}$ and $\Delta_n \in \{\pm \frac{2\pi n}{N}\}_{n \in \mathcal{N}}$, respectively.

Next, we define

$$\chi_n(\Delta_m, \Delta_n) := I_\Lambda(n) \frac{1}{K} \sum_{k=0}^{K-1} e^{-j \Delta_m c_{n,k} - j \Delta_n n}, \quad (41)$$

where the random variable $I_\Lambda(n)$ satisfies $I_\Lambda(n) = 1$ when $n \in \Lambda$ and 0 otherwise. In addition, let

$$\chi(\Delta_m, \Delta_n) := \sum_{n=0}^{N-1} \chi_n(\Delta_m, \Delta_n). \quad (42)$$

Some of the magnitudes $|\chi(\Delta_m, \Delta_n)|$ are duplicated since $\chi(\Delta_m, \Delta_n) = \chi(\Delta_m \pm 2\pi, \Delta_n \pm 2\pi)$ and $\chi(\Delta_m, \Delta_n) = \chi^*(-\Delta_m, -\Delta_n)$. To eliminate the duplication and remove the trivial nonrandom value $\chi(0, 0)$, we restrict the values of Δ_m and Δ_n to $\Delta_m \in \{\frac{2\pi m}{M}\}_{m \in \mathcal{M}}$ and $\Delta_n \in \{\frac{2\pi n}{N}\}_{n \in \mathcal{N}}$, respectively, and define the set

$$\Xi := \{(\Delta_m, \Delta_n) \mid (m, n) \in \mathcal{M} \times \mathcal{N} \setminus (0, 0)\}, \quad (43)$$

with cardinality $|\Xi| = MN - 1$, such that each value of $|\Phi_*|_{l_1}^H [\Phi_*]_{l_2}|$ (except the trivial case $l_1 = l_2$) corresponds to a single element of the set Ξ . We can now write (40) as

$$\mu(\Phi_*) = \max_{(\Delta_m, \Delta_n) \in \Xi} \frac{1}{|\Lambda|} |\chi(\Delta_m, \Delta_n)|. \quad (44)$$

The coherence in (44) is a function of the dependent random variables χ and $|\Lambda|$. To bound μ , we derive bounds on χ and $|\Lambda|$, respectively. To this aim, we first characterize the statistical moments of $\chi_n(\Delta_m, \Delta_n)$ for some fixed $(\Delta_m, \Delta_n) \in \Xi$, which we denote henceforth as χ_n , in the following lemma:

Lemma 3. *The sequence of random variables $\{\chi_n\}$ satisfies*

$$E[\chi_n] = \begin{cases} ue^{j\Delta_n n}, & \text{if } \Delta_m = 0, \\ 0, & \text{otherwise,} \end{cases} \quad (45)$$

$$\sum_{n=0}^{N-1} D[\chi_n] = \begin{cases} u(1-u)N, & \text{if } \Delta_m = 0, \\ \frac{M-K}{(M-1)K}uN, & \text{otherwise.} \end{cases} \quad (46)$$

Furthermore, for each $n \in \mathcal{N}$,

$$|\chi_n - E[\chi_n]| \leq 1, \quad \text{w.p. 1.} \quad (47)$$

Proof. See Appendix B. \square

Using Lemma 3, the probability that the magnitude $|\chi|$ is bounded can be derived as in the following Corollary:

Corollary 4. *Let $V := \max \left\{ u(1-u)N, \frac{M-K}{(M-1)K}uN \right\}$. For any $(\Delta_m, \Delta_n) \in \Xi$ and $\epsilon \leq V$ it holds that*

$$\mathbb{P}(|\chi| \geq \sqrt{V} + \epsilon) \leq e^{-\frac{\epsilon^2}{4V}}. \quad (48)$$

Proof. Based on the definition (41) and the independence assumption on the frequency selection and missing-or-not status of each pulse, it holds that $\{\chi_n - E[\chi_n]\}_{n \in \mathcal{N}}$ are independent zero-mean complex-valued random variables. Now, since

$$\sum_{n=0}^{N-1} E[\chi_n] = \begin{cases} u \sum_{n=0}^{N-1} e^{j\Delta_n n}, & \text{if } \Delta_m = 0, \\ 0, & \text{otherwise,} \end{cases} \quad (49)$$

according to (45) and $\sum_{n=0}^{N-1} e^{j\Delta_n n} = \frac{1 - e^{j\Delta_n N}}{1 - e^{j\Delta_n}}$ equals 0 for $\Delta_n \in \{\frac{2\pi n}{N}\}_{n \in \mathcal{N} \setminus \{0\}}$, recalling that $(\Delta_m, \Delta_n) \neq (0, 0)$, we have $\sum_{n=0}^{N-1} E[\chi_n] = 0$. Then, it holds that $\sum_{n=0}^{N-1} (\chi_n - E[\chi_n]) = \sum_{n=0}^{N-1} \chi_n = \chi$. Combining Bernstein's inequality [27, Thm. 12] with the fact that by (47), $|\chi_n - E[\chi_n]| \leq 1$, results in (48). \square

We next derive a bound on the number of effective pulses $|\Lambda|$ in the following lemma:

Lemma 5. *For any $t > 0$, it holds that*

$$\mathbb{P}(|\Lambda| \leq uN - t) < e^{-\frac{2t^2}{N}}. \quad (50)$$

Proof. Since, by its definition, $|\Lambda|$ obeys a binomial distribution, (50) is a direct consequence of [28, Thm. 1]. \square

Based on the requirement $\mu(\Phi_*) > \frac{1}{2K-1}$ in Theorem 2, we now use Corollary 4 and Lemma 5 to derive a sufficient condition on the radar parameters M , N , K , as well as the intensity of interference $1 - u$, guaranteeing that the

measurement matrix Φ_* meets the requirement with high probability. This condition is stated in the following theorem:

Theorem 6. For any constant $\delta > 0$, the coherence of Φ_* satisfies $\mathbb{P}\left(\mu(\Phi_*) \leq \frac{1}{2S-1}\right) \geq 1 - \delta$ when

$$S \leq \frac{uN/\sqrt{V}}{1 + \sqrt{2(\log 2|\Xi| - \log \delta)}} \frac{1 + \frac{1}{2\sqrt{2N}u}}{2} - \sqrt{\frac{N}{32V}} + \frac{1}{2}. \quad (51)$$

Proof. See Appendix C. \square

Recall that the value of V depends on the quantities u , K and M . When u is reasonably large such that $1-u \geq \frac{M-K}{(M-1)K}$, we have $V = \frac{M-K}{(M-1)K}uN$. When there is no noise in radar returns, a number of scattering points (on the grid) in the scale of $S = O\left(\sqrt{\frac{KuN}{\log MN}}\right)$ guarantees a unique reconstruction of range-Doppler parameters with high probability according to Theorems 2 and 6. Note that this rather simple asymptotic condition assumes that $\frac{M-1}{M-K} \approx 1$, i.e., that the overall number of available frequencies M is substantially larger than the number of frequencies utilized in each pulse K , thus ensuring the agile character in frequency domain. Compared to the asymptotic condition $O\left(\sqrt{\frac{N}{\log MN}}\right)$ of FAR with full observations [7], we find that the presence of corrupted observations, i.e. when $u < 1$, leads to degraded range-Doppler reconstruction performance. However, by increasing the number of transmitted frequencies in each pulse K while maintaining $K \ll M$, the performance deterioration due to missing observations can be mitigated, enhancing the interference immunity of the radar in extreme electromagnetic environments. In the special case that $K = 1$ and $u = 1$, i.e., FAR in an interference free environment, the two conditions coincide as $O\left(\sqrt{\frac{KuN}{\log MN}}\right) = O\left(\sqrt{\frac{N}{\log MN}}\right)$.

The above condition is proposed for the noiseless case, indicating that the inherent target reconstruction capacity increases with \sqrt{K} . In practical noisy cases, the reconstruction performance does not monotonically increase with K , because the transmit power of each frequency decreases with K , thus degrading the signal-to-noise ratio (SNR) in both CAESAR and WMAR. Particularly, in CAESAR, larger K means that less antennas (L/K) are allocated to each frequency, which affects the radiation beam and enlarges the gain loss. In addition, a small K maintains the practical advantages of frequency agility in terms of, e.g., ECCM and EMC performance.

VII. SIMULATION RESULTS

In this section, we numerically compare the performance of WMAR, CAESAR, and FAR in noiseless, noisy, and jamming environments. In the presence of jamming, both missing patterns, i.e., 1) pulse selective and 2) observation selective, are tested with the same value of u , which represents the probability of missing a pulse in 1) or an observation in 2). The results for these patterns using CAESAR and WMAR are denoted by CAESAR1/CAESAR2 and WMAR1/WMAR2, respectively. Note that in FAR, the two patterns coincide.

We consider a frequency band starting from $f_c = 9$ GHz, with $M = 8$ available carriers and carrier spacing of $\Delta f = 1$ MHz. The radar system is equipped with an antenna array

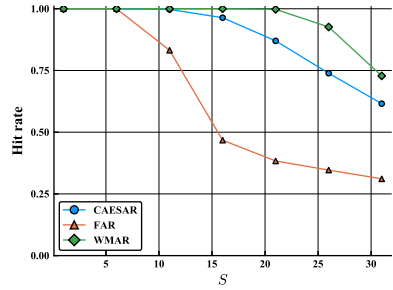


Fig. 2. Range-Doppler recovery versus S , noiseless setting.

of $L = 10$ elements with spacing of $d = \frac{c}{2f_c}$, and utilizes $N = 32$ pulses focusing on $\theta = 0$. CAESAR and WMAR use $K = 2$ frequencies at each pulse. The numerical performance is averaged over 100 Monte Carlo trials. In each trial, the range-Doppler parameters of each target are randomly chosen from the grid points, and the angle ϑ is randomly set within the beam $\vartheta \in \Theta$. The scattering intensities are set to 1.

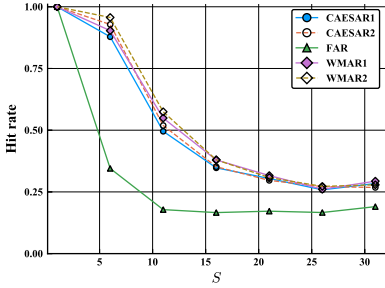
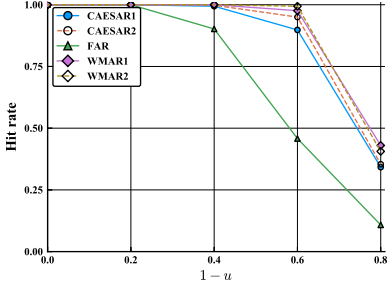
In order to implement target recovery via Algorithm 1 for the three radar schemes, we use the convex optimization toolbox [29] to implement basis pursuit (36) in noiseless cases or Lasso algorithm in noisy setups for range-Doppler reconstruction, using hit rate as the criterion. A hit is proclaimed if the range-Doppler parameter of a scattering point is successfully recovered. Using the recovered range-Doppler parameters, the angles are estimated, and we calculate the root mean squared error (RMSE) of the recovered scattering points, $\sqrt{\mathbb{E}[(\vartheta_s - \hat{\vartheta}_s)^2]}$, for $s \in \mathcal{S} \cap \hat{\mathcal{S}}$, as the performance metric.

A. Noiseless Cases

We first evaluate the proposed radar schemes in a noiseless setup. In the first experiment, we simulate different numbers of recoverable scattering points, S . The resulting hit rates versus $S \in \{1, \dots, N-1\}$ are depicted in Fig. 2. As expected, the hit rates decrease as S increases. The performance of CAESAR is within a very small gap of that achievable using WMAR, because CAESAR and WMAR use the same amount of transmitted frequencies K , and the number of beamformed measurements is also the same. Hit rates of CAESAR and WMAR exceed that of FAR significantly. This gain stems from the fact that transmitting multi-carriers in each pulse of CAESAR and WMAR increases the number of observations, and thus raises the number of recoverable scattering points.

We next consider a jamming environment with survival rate $u = 0.4$. The resulting hit rates evaluated for this setup are depicted in Fig. 3. Comparing Figs. 2 and 3, we see that the hit rates of all radar schemes are degraded due to jamming. In the presence of jamming, CAESAR achieves roughly the same performance as costly WMAR, indicating the gains of spatial agility in such environments. In particular, for both missing patterns, CAESAR and WMAR have close hit rates and outperform FAR significantly, owing to the increased number of transmitting frequencies.

Finally, we fix $S = 5$ and vary the pulse/observation survival rate u to examine the robustness of the radars to the jamming intensities. The hit rate results are depicted in Fig. 4, which again demonstrates the increased robustness of CAESAR and WMAR. Here, CAESAR achieves roughly

Fig. 3. Range-Doppler recovery versus S , jamming scenario.Fig. 4. Range-Doppler recovery versus the missing rates $1 - u$.

the same performance as WMAR for all considered jamming profiles, and significantly outperforms FAR.

B. Noisy Cases

Here, we consider the case where the data matrix/cube is corrupted by additive i.i.d. zero-mean proper-complex Gaussian noise with variance κ^2 . We let the SNR, defined as $1/\kappa^2$, vary, examining its impact on the radars performance. The radar setting are the same as in the noiseless case.

In the first experiment, we consider the a jamming free case, and set $S = 12$. The hit rates of the range-Doppler parameters and RMSE in angle estimation are depicted in Figs. 5-6, respectively. Observing Figs. 5-6, we note that, as expected, WMAR achieves the best performance in both range-Doppler reconstruction and angle estimation. While WMAR and CAESAR have the same number of observations, CAESAR has a

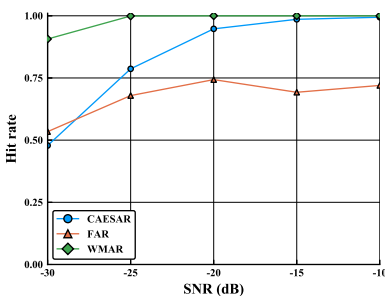


Fig. 5. Range-Doppler recovery versus SNR.

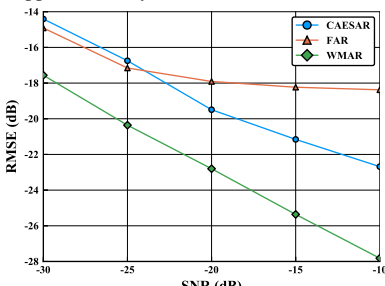


Fig. 6. Angle estimation performance versus SNR.

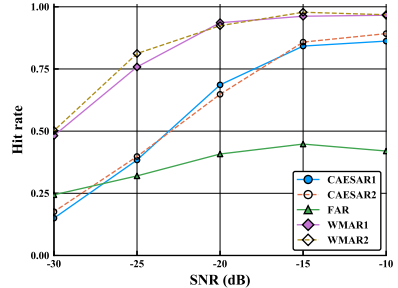


Fig. 7. Range-Doppler recovery versus SNR, jamming scenario.

lower antenna gain as noted in Subsection V-A, which results in its degraded performance compared to WMAR. In high SNRs, i.e., $\text{SNR} \geq -25$ dB, CAESAR has higher hit rates than FAR due to the advantage of increased number of transmitted frequencies. In low SNRs of less than -30 dB, both CAESAR and FAR become unstable (with hit rates around or lower than 0.5), and FAR exceeds CAESAR owing to its higher antenna gain. Note that the RMSE is calculated only for those successfully recovered scattering points and depends mainly on SNR. We find that FAR has slightly higher accuracy than CAESAR in low SNR scenarios, because CAESAR has a K^2 loss factor in the amplitudes of received echoes in comparison with FAR after receive beamforming. WMAR, whose amplitude loss compared to FAR is only by a factor of \sqrt{K} , achieves the best hit rates.

Finally, we consider a jamming environment and let $u = 0.4$. The number of scattering points is set to $S = 5$. The hit rates of the range-Doppler parameters are depicted in Fig. 7. In this scenario, we note that WMAR has the highest hit rates, CAESAR ranks the second, and that FAR almost fails to reconstruct scattering points (with hit rates less than 0.5). The superiority of WMAR/CAESAR over FAR demonstrates the advantage of the proposed multi-carrier waveforms. Comparing WMAR and CAESAR shows the tradeoff induced by array allocation in CAESAR, which allows to trade hardware complexity for a controllable loss in antenna gain.

From the experimental results in both noiseless and noisy cases, we find that the multi-carrier signals used by CAESAR and WMAR significantly enhance range-Doppler reconstruction performance over the monotone waveform in traditional FAR. The advantage becomes more distinct in jamming environments, where some radar measurements are invalid. In reasonably high SNR scenarios, the hit rates of CAESAR, which uses constant modulus waveforms, approach those of WMAR, which uses costly wideband waveforms.

VIII. CONCLUSION

In this work we developed two multi-carrier frequency agile schemes for phase array radars: WMAR, which uses wideband waveform; and CAESAR, which transmits monotone signals and introduces spatial agility. We modeled the received radar signal, and proposed an algorithm for target recovery. We then characterized theoretical recovery guarantees. Our numerical results demonstrate that our proposed schemes achieve enhanced survivability in extreme electromagnetic environments. Furthermore, it is shown that CAESAR is capable of achieving performance which approaches that of costly wideband radar,

while utilizing low-cost narrowband transceivers. An additional benefit which follows from the introduction of frequency and spatial agility is the natural implementation of CAESAR as a DFRC system, studied in a companion paper.

APPENDIX

A. Proof of Lemma 1

In the following we prove (24) for CAESAR. The proof for WMAR follows similar arguments and is omitted for brevity.

Substituting the definitions of \mathbf{w} , \mathbf{P} and \mathbf{Y} into (23) yields

$$\begin{aligned} Z_{k,n} &= \sum_{l=0}^{L-1} w_l(\theta, \Omega_{n,k}) [\mathbf{p}(n, k)]_l \sum_{s=0}^{S-1} \tilde{\beta}_s e^{j\tilde{r}_s c_{n,k}} \\ &\quad e^{j\tilde{v}_s n \zeta_{n,k}} e^{-j2\pi\Omega_{n,k} l d \sin \vartheta_s / c} \rho_C(n, k, \delta_{\vartheta_s}) \\ &= \sum_{s=0}^{S-1} \sum_{l=0}^{L-1} [\mathbf{p}(n, k)]_l \tilde{\beta}_s e^{j\tilde{r}_s c_{n,k}} e^{j\tilde{v}_s n \zeta_{n,k}} \\ &\quad e^{-j2\pi\Omega_{n,k} l d (\sin \vartheta_s - \sin \theta) / c} \rho_C(n, k, \delta_{\vartheta_s}) \\ &= \sum_{s=0}^{S-1} \tilde{\beta}_s e^{j\tilde{r}_s c_{n,k}} e^{j\tilde{v}_s n \zeta_{n,k}} \rho_C^2(n, k, \delta_{\vartheta_s}). \quad (\text{A.1}) \end{aligned}$$

Recall that when $\delta_{\vartheta_s} \approx 0$ it holds that $\rho_C(n, k, \delta_{\vartheta_s}) \approx L/K = \sqrt{\alpha_K}$. Then, (A.1) reduces to (24), proving the lemma. \square

B. Proof of Lemma 3

We first prove (45) and (46), after which we address (47).

1) *Proof of (45) and (46):* For brevity, let $p = -\Delta_m$, $q = -\Delta_n$, $I_n = I_\Lambda(n)$, and $B = \binom{M}{K}$. We set $\binom{M}{K} = 0$ when $M \leq 0$ or $K < 0$, and $\binom{M}{0} = 1$ when $M > 0$.

We first compute $E[\chi_n] = \frac{1}{K} E[I_n e^{jqn} \sum_{k=0}^{K-1} e^{jpc_{n,k}}]$. The expectation is taken over the indicator I_n and frequency codes $c_{n,k}$. Since they are independent and $E[I_n] = u$, it holds that

$$E[\chi_n] = \frac{ue^{jqn}}{K} E \left[\sum_{k=0}^{K-1} e^{jpc_{n,k}} \right]. \quad (\text{B.1})$$

Since K frequencies are selected uniformly (but not independently), it follows that

$$E \left[\sum_{k=0}^{K-1} e^{jpc_{n,k}} \right] = \frac{1}{B} \sum_{i=0}^{B-1} \sum_{k=0}^{K-1} e^{jpm_{i,k}}, \quad (\text{B.2})$$

where $m_{i,k}$ denotes the k -th frequency in the i -th combination. Out of these B combinations, there are $\binom{M-1}{K-1}$ that contain a given selection $m \in \mathcal{M}$. Thus, we have that

$$\sum_{i=0}^{B-1} \sum_{k=0}^{K-1} e^{jpm_{i,k}} = \binom{M-1}{K-1} \sum_{m=0}^{M-1} e^{jpm} = \frac{BK}{M} \sum_{m=0}^{M-1} e^{jpm}. \quad (\text{B.3})$$

Substituting (B.3) into (B.2) yields

$$E \left[\sum_{k=0}^{K-1} e^{jpc_{n,k}} \right] = \frac{K}{M} \sum_{m=0}^{M-1} e^{jpm} = \frac{K}{M} \frac{1 - e^{jpM}}{1 - e^{jp}}. \quad (\text{B.4})$$

As $p \in \left\{ \frac{2\pi m}{M} \right\}_{m \in \mathcal{M}}$, it holds that $E \left[\sum_{k=0}^{K-1} e^{jpc_{n,k}} \right] = K$ if $p = 0$ and zero otherwise. Substituting this into (B.1), we have

$$E[\chi_n] = \begin{cases} ue^{jqn}, & \text{if } p = 0, \\ 0, & \text{otherwise,} \end{cases} \quad (\text{B.5})$$

which proves (45).

To obtain $D[\chi_n] := E[|\chi_n - E[\chi_n]|^2]$, we consider two cases, $p = 0$ and $p \neq 0$. When $p = 0$, we have $\chi_n = I_n e^{jqn}$ and

$$\begin{aligned} E \left[|I_n e^{jqn} - ue^{jqn}|^2 \right] &= E[(I_n - u)^2] \\ &\stackrel{(a)}{=} E[I_n + u^2 - 2I_n u] \stackrel{(b)}{=} u - u^2, \end{aligned} \quad (\text{B.6})$$

where (a) holds since $I_n^2 = I_n$ and in (b) we apply $E[I_n] = u$.

When $p \neq 0$, the random variable χ_n has zero mean, and its variance is given by

$$\begin{aligned} E[|\chi_n|^2] &= E \left[\frac{I_n}{K} \left| \sum_{k=0}^{K-1} e^{jpc_{n,k} + jqn} \right|^2 \right] \\ &= \frac{1}{K^2} E \left[I_n \cdot \sum_{k=0}^{K-1} \sum_{k'=0}^{K-1} e^{jp(c_{n,k} - c_{n,k'})} \right] \\ &= \frac{u}{K^2} E \left[\sum_{k=0}^{K-1} \sum_{k'=0}^{K-1} e^{jp(c_{n,k} - c_{n,k'})} \right], \end{aligned} \quad (\text{B.7})$$

where we use $I_n^2 = I_n$. To compute (B.7), we note that

$$\begin{aligned} E \left[\sum_{k=0}^{K-1} \sum_{k'=0}^{K-1} e^{jpc_{n,k} - jpc_{n,k'}} \right] &= \frac{\binom{M-1}{K-1}}{B} \sum_{m=0}^{M-1} e^{jp \cdot 0} + \frac{\binom{M-2}{K-2}}{B} \sum_{m=0}^{M-1} \sum_{m'=0, m' \neq m}^{M-1} e^{jp(m-m')} \\ &\stackrel{(a)}{=} \frac{\binom{M-1}{K-1} - \binom{M-2}{K-2}}{B} M + \frac{\binom{M-2}{K-2}}{B} \sum_{m=0}^{M-1} \sum_{m'=0}^{M-1} e^{jp(m-m')}, \end{aligned} \quad (\text{B.8})$$

where (a) follows since $\sum_{m=0}^{M-1} \sum_{m'=0, m' \neq m}^{M-1} e^{jp(m-m')}$ in the second term can be replaced by $\sum_{m=0}^{M-1} \sum_{m'=0}^{M-1} e^{jp(m-m')} - \sum_{m=0}^{M-1} e^0$. From the derivation of (B.5), it holds that for $p \neq 0$ the second summand in (B.8) vanishes, resulting in

$$E \left[\sum_{k=0}^{K-1} \sum_{k'=0}^{K-1} e^{jpc_{n,k} - jpc_{n,k'}} \right] = \frac{(M-K)K}{M-1}. \quad (\text{B.9})$$

Plugging (B.9) into (B.7), we obtain

$$E[|\chi_n|^2] = \frac{M-K}{(M-1)K} u, \quad \text{if } p \neq 0. \quad (\text{B.10})$$

Finally, to prove (46), we calculate $\sum_{n=0}^{N-1} D[\chi_n]$ for $p = 0$ and $p \neq 0$. When $p = 0$, from (B.6), we have that

$$\sum_{n=0}^{N-1} D[\chi_n] = \sum_{n=0}^{N-1} (u - u^2) = (u - u^2) N. \quad (\text{B.11})$$

When $p \neq 0$, it follows from (B.10) that

$$\sum_{n=0}^{N-1} D[\chi_n] = \frac{M-K}{(M-1)K} u N. \quad (\text{B.12})$$

Combining (B.11) and (B.12) proves (46). \square

2) *Proof of (47):* We again consider the two cases $p = 0$ and $p \neq 0$ separately: When $p = 0$, it follows from (B.5) that

$$\begin{aligned} |\chi_n - \mathbb{E}[\chi_n]|^2 &= |(I_n - u) e^{jgn}|^2 = (I_n - u)^2 \\ &= \begin{cases} (1 - u)^2 \leq 1, & \text{if } I_n = 1, \\ u^2 \leq 1, & \text{otherwise.} \end{cases} \end{aligned} \quad (\text{B.13})$$

When $p \neq 0$, $|\chi_n - \mathbb{E}[\chi_n]|^2 = |\chi_n|^2$, which is not larger than 1 by definition of χ_n (41), thus proving (47). \square

C. Proof of Theorem 6

By fixing some positive $\epsilon \leq V$, setting $t = \sqrt{\frac{N}{8V}}\epsilon$ and

$$\epsilon' := \frac{\sqrt{V} + \epsilon}{uN - \sqrt{\frac{N}{8V}}\epsilon} = \frac{\sqrt{V} + \epsilon}{uN - t}, \quad (\text{C.1})$$

we have that for any $(\Delta_m, \Delta_n) \in \Xi$

$$\begin{aligned} \mathbb{P}\left(\frac{|\chi|}{|\Lambda|} \geq \epsilon'\right) &\stackrel{(a)}{\leq} \mathbb{P}\left(|\chi| \geq \sqrt{V} + \epsilon \cup |\Lambda| \leq uN - t\right) \\ &\leq \mathbb{P}\left(|\chi| \geq \sqrt{V} + \epsilon\right) + \mathbb{P}\left(|\Lambda| \leq uN - t\right) \\ &\stackrel{(b)}{\leq} 2e^{-\frac{\epsilon^2}{4V}}. \end{aligned} \quad (\text{C.2})$$

Here (a) holds since the event $\frac{|\chi|}{|\Lambda|} \geq \frac{\sqrt{V} + \epsilon}{uN - t}$ implies that at least one of the conditions $|\chi| \geq \sqrt{V} + \epsilon$ and $|\Lambda| \leq uN - t$ is satisfied; and (b) follows from Corollary 4 and Lemma 5.

Using the bound (C.2) on the magnitude of the normalized correlation, we next bound the probability of $\mu(\Phi_*)$ to exceed some constant. By applying the union bound to (44), we have

$$\begin{aligned} \mathbb{P}(\mu(\Phi_*) \geq \epsilon') &\leq \sum_{(\Delta_m, \Delta_n) \in \Xi} \mathbb{P}\left(\frac{|\chi(\Delta_m, \Delta_n)|}{|\Lambda|} > \epsilon'\right) \\ &\leq 2|\Xi|e^{-\frac{\epsilon^2}{4V}}. \end{aligned} \quad (\text{C.3})$$

According to (C.3), for any $\epsilon > 0$, it holds that

$$\mathbb{P}(\mu(\Phi_*) \leq \epsilon') \geq 1 - 2|\Xi|e^{-\frac{\epsilon^2}{4V}}, \quad (\text{C.4})$$

where ϵ' is obtained from ϵ via (C.1). The right hand side of (C.4) is not smaller than $1 - \delta$ when $\delta \geq 2|\Xi|e^{-\frac{\epsilon^2}{4V}}$, implying that $\mathbb{P}(\mu(\Phi_*) \leq \epsilon') \geq 1 - \delta$ when ϵ satisfies

$$\epsilon \geq \sqrt{2V(\log 2|\Xi| - \log \delta)}. \quad (\text{C.5})$$

Finally, by (C.1), fixing $\epsilon' = 1/(2S - 1)$ implies that

$$S = \frac{uN - \sqrt{\frac{N}{8V}}\epsilon}{2\sqrt{V} + 2\epsilon} + \frac{1}{2} = \frac{uN + \sqrt{N/8}}{2\sqrt{V} + 2\epsilon} - \sqrt{\frac{N}{32V}} + \frac{1}{2}. \quad (\text{C.6})$$

Substituting (C.5) into (C.6) proves (51). \square

REFERENCES

- [1] S. R. J. Axelsson, "Analysis of random step frequency radar and comparison with experiments," *IEEE Trans. Geosci. Remote Sens.*, vol. 45, no. 4, pp. 890–904, April 2007.
- [2] J. Yang, J. Thompson, X. Huang, T. Jin, and Z. Zhou, "Random-frequency SAR imaging based on compressed sensing," *IEEE Trans. Geosci. Remote Sens.*, vol. 51, no. 2, pp. 983–994, 2013.
- [3] C. Hu, Y. Liu, H. Meng, and X. Wang, "Randomized Switched Antenna Array FMCW Radar for Automotive Applications," *IEEE Trans. Veh. Technol.*, vol. 63, no. 8, pp. 3624–3641, oct 2014.
- [4] Y. Liu, G. Liao, J. Xu, Z. Yang, and Y. Zhang, "Adaptive OFDM integrated radar and communications waveform design based on information theory," *IEEE Commun. Lett.*, vol. 21, no. 10, pp. 2174–2177, Oct 2017.
- [5] D. Cohen, K. V. Mishra, and Y. C. Eldar, "Spectrum sharing radar: Coexistence via Xampling," *IEEE Trans. Aerosp. Electron. Syst.*, vol. 54, no. 3, pp. 1279–1296, 2018.
- [6] T. Huang, Y. Liu, G. Li, and X. Wang, "Randomized stepped frequency ISAR imaging," in *Proc. IEEE RadarConf*, May 2012, pp. 0553–0557.
- [7] T. Huang, Y. Liu, X. Xu, Y. C. Eldar, and X. Wang, "Analysis of Frequency Agile Radar via Compressed Sensing," *IEEE Trans. Signal Process.*, vol. 66, no. 23, pp. 6228–6240, Dec 2018.
- [8] T. Huang, Y. Liu, Y. C. Eldar, and X. Wang, "Multiple carrier agile radar via compressed sensing," in *Proc. IEEE CoSeRa*, 2018.
- [9] Y. Wang, J. Li, and P. Stoica, *Spectral Analysis of Signals: The Missing Data Case*. Morgan & Claypool, 2006.
- [10] W. Rao, G. Li, X. Wang, and X. Xia, "ISAR imaging of maneuvering targets with missing data via matching pursuit," in *Proc. IEEE RadarCon*, May 2011, pp. 124–128.
- [11] H. Sun, F. Brigui, and M. Lesturgie, "Analysis and comparison of MIMO radar waveforms," in *2014 International Radar Conference*, Oct 2014.
- [12] D. Cohen, D. Cohen, Y. C. Eldar, and A. M. Haimovich, "SUMMeR: Sub-Nyquist MIMO Radar," *IEEE Trans. Signal Process.*, vol. 66, no. 16, pp. 4315–4330, Aug 2018.
- [13] P. Antonik, M. C. Wicks, H. D. Griffiths, and C. J. Baker, "Frequency diverse array radars," in *2006 IEEE Conference on Radar*, April 2006.
- [14] Y. Liu, H. Ruan, L. Wang, and A. Nehorai, "The Random Frequency Diverse Array: A New Antenna Structure for Uncoupled Direction-Range Indication in Active Sensing," *IEEE J. Sel. Topics Signal Process.*, vol. 11, no. 2, pp. 295–308, mar 2017.
- [15] E. Brookner, "MIMO radar demystified and where it makes sense to use," in *2013 IEEE International Symposium on Phased Array Systems and Technology*, Oct 2013, pp. 399–407.
- [16] S. Chen and F. Xi, "Quadrature compressive sampling for multiband radar echo signals," *IEEE Access*, vol. 5, pp. 19742–19760, 2017.
- [17] A. Hassanien, M. G. Amin, Y. D. Zhang, and F. Ahmad, "Phase-modulation based dual-function radar-communications," *IET Radar, Sonar Navigation*, vol. 10, no. 8, pp. 1411–1421, 2016.
- [18] C. Sturm and W. Wiesbeck, "Waveform Design and Signal Processing Aspects for Fusion of Wireless Communications and Radar Sensing," *Proc. IEEE*, vol. 99, no. 7, pp. 1236–1259, Jul 2011.
- [19] D. Ma, T. Huang, Y. Liu, and X. Wang, "A novel joint radar and communication system based on randomized partition of antenna array," in *Proc. IEEE ICASSP*, April 2018, pp. 3335–3339.
- [20] T. Huang, N. Shlezinger, X. Xu, Y. Liu, and Y. C. Eldar, "A dual-function radar communication system using index modulation," in *Proc. IEEE SPAWC*, 2019.
- [21] S. U. Pillai, *Array Signal Processing*, C. S. Burrus, Ed. Springer, 1989.
- [22] M. A. Richards, *Fundamentals of radar signal processing*. Tata McGraw-Hill Education, 2005.
- [23] Y. C. Eldar and G. Kutyniok, *Compressed Sensing: Theory and Applications*. Cambridge University Press, 2012.
- [24] Y. C. Eldar, *Sampling theory: Beyond bandlimited systems*. Cambridge University Press, 2015.
- [25] J. Fuchs, "On sparse representations in arbitrary redundant bases," *IEEE Trans. Inform. Theory*, vol. 50, no. 6, pp. 1341–1344, June 2004.
- [26] D. S. Pham and A. M. Zoubir, "Estimation of multicomponent polynomial phase signals with missing observations," *IEEE Transactions on Signal Processing*, vol. 56, no. 4, pp. 1710–1715, April 2008.
- [27] D. Gross, "Recovering low-rank matrices from few coefficients in any basis," *IEEE Transactions on Information Theory*, vol. 57, no. 3, pp. 1548–1566, March 2011.
- [28] M. Okamoto, "Some inequalities relating to the partial sum of binomial probabilities," *Annals of the Institute of Statistical Mathematics*, vol. 10, no. 1, pp. 29–35, Mar 1959.
- [29] M. Udell, K. Mohan, D. Zeng, J. Hong, S. Diamond, and S. Boyd, "Convex optimization in Julia," *SC14 Workshop on High Performance Technical Computing in Dynamic Languages*, 2014.